Progress in Additive Manufacturing
https://doi.org/10.1007/s40964-025-01021-8

FULL RESEARCH ARTICLE

A finite element approach for modelling the fracture behaviour of unidirectional FFF-printed parts

Simon Seibel[1] · **Josef Kiendl**[1]

Received: 19 September 2024 / Accepted: 8 February 2025

Abstract
We present a finite element modelling approach for unidirectional Fused Filament Fabrication (FFF)-printed specimens under tensile loading. In this study, the focus is on the fracture behaviour, the goal is to simulate the mechanical behaviour of specimens with different strand orientations until final failure of the specimens. In particular, the aim is to represent experimentally observed failure modes for different print orientations and the typical dependence of the parts' strength on the print orientation. We investigate several modelling aspects like the choice of a suitable failure criterion, a suitable way to represent fracture in the finite element mesh or the necessary level of detail when modelling the characteristic edges of FFF-printed specimens. As a result, this work provides an approach to model FFF printed specimens in finite element simulations, which can represent the characteristic relation between mesostructural layout and macroscopic fracture behaviour.

Keywords 3D printing · Fused Filament Fabrication · Additive manufacturing · Structural mechanics · Finite element analysis · Fracture

1 Introduction

Additive manufacturing (AM) has found its way into rapid prototyping and the production of small quantities like spare parts in particular. After creating a geometry in a CAD software, a 3D surface is generated. This surface is processed by a so-called slicer software into a G-code, which contains all the commands for the printing process. There are various techniques to print the parts, including Fused Filament Fabrication (FFF), which is the focus of the following studies. In FFF printing, the mechanical properties of the printed part depend without consideration of lattice structures at the macro level, as shown, for example, in [1], on many parameters, such as the printing speed, the printing material, the bed temperature, the printing temperature, ageing, the type of retraction and the spacing of the strands [2–7]. In particular, the mechanical properties in FFF depend on the layer orientation, which numerous studies [8–14] have shown experimentally. The main result of these studies with a unidirectional layer structure of the tensile specimens states that e.g. the tensile strength is highest if the strand direction is equal to the loading direction and lowest if the strand direction is orthogonal to the loading direction. This effect, that the tensile strength and stiffness decrease with increasing angle between strand orientation and loading direction, was also shown partly in FE simulations, that can be divided in two methods. In principle, there are methods of homogenised models, for example using a representative volume element (RVE) or classical laminate theory (CLT) theory [15, 16] or models, that resolve the micro-/mesostructure [17, 18] to predict the mechanical properties. Models using a RVE or CLT can model the stiffness and failure as a function of different angles by determining the material parameters for each configuration from several reference tests and then simulating (parts of) the tensile specimen. In contrast to the models using anisotropic material parameters, the number of material parameters as input for models can be reduced by resolving the mesostructure. Only the structure of the strands with the same (isotropic) material parameters for every configuration results in different mechanical properties on a macroscopic level. [19], for example, simulates the complex behaviour of the mesostructure using an elasto-plastic

✉ Simon Seibel
simon.seibel@unibw.de

Josef Kiendl
josef.kiendl@unibw.de

[1] Institute of Engineering Mechanics and Structural Analysis, Universität der Bundeswehr München, Werner-Heisenberg-Weg 39, 85577 Neubiberg, Germany

Published online: 25 February 2025

approach, but the failure is not simulated. The number of homogenised models outnumbers models that resolve the individual strands and failure of the specimen itself was simulated in none of the mentioned studies. This is where this work starts and simulating the failure in the Finite Element Analysis (FEA) to show the dependency of the angle between strands and the loading direction and simulation of the failure on a mesostructure scale. The advantage of modelling the specimens using individual strands is the outcome of realistic failure patterns and the lower input of material parameters, as the effect of the different orientations is provided by the strand's geometry and orientation in relation to the loading direction. Therefore, the results of [8] are used in this study, as not only the angles 0°, 45° and 90° were experimentally investigated here, but also angles in between. The aim is to numerically simulate the mechanical behaviour of unidirectional FFF-printed specimens with different print orientations until final failure, representing the experimentally observed failure modes and the typical dependence of the parts' strength on the print orientation.

2 Materials and methods

2.1 FFF printing

In this section, the basic features of the FFF printing process and the resulting mesostructure, which are shown schematically in Fig. 1, and its impact on the mechanical material behaviour of the printed part are discussed.

In the FFF process, a thermoplastic filament is melted from a coil through a heated nozzle and then deposited on a print bed along a predefined path. This procedure is repeated layer by layer until the object is fully printed. Typically, a layer is printed continuously so that the (mostly parallel) strands are always connected at one end. This could have an influence on the type and the initiation of failure. Due to the dependency of the mechanical properties on the print orientation, the layers are typically printed alternately at a 90° angle in order to minimise these dependencies and to ensure that the failure does not depend too much on the print orientation. In this work, we want to focus on precisely this resulting anisotropy and print the tensile specimens with a unidirectional layup. Typical for the printing process are the air gaps between the strands shown in Fig. 2. The strands touch each other on all sides, but not over the entire width or height due to the air gaps, which also has an influence on the failure.

The direction of the strands can be varied as required for one and the same object. This resulting anisotropy, which comes purely from the printing process, has a considerable influence on the mechanical properties of the object as mentioned above. As an example, in addition to the studies mentioned in Sect. 1, Fig. 3 shows the stress–strain-diagram for a tensile test with different angles of the deposited strands relative to the tensile direction. The decreasing strength and stiffness with increasing angle are clearly recognisable. The specimens in [8] were printed on a Raise3D Pro2 printer with a extruder width of 0.4 mm and PLA filament from EasyPrint was used. Printing speed was set to 30 $\frac{\text{mm}}{\text{s}}$. No contour were used, which would have a potential influence on the layers. The extruder temperature was set to 200 °C, the bed temperature to 60 °C. For further details, reference is made to [8]. The experiments from [8], shown in Fig. 3, are compared and discussed with the numerical model presented in this paper.

Additionally, the polymer strand can consist of different materials such as acrylonitrile butadiene styrene (ABS), polyether ether ketone (PEEK) or polylactic acid (PLA), which

Fig. 2 Schematic section through the printed object with two layers printed in the same direction

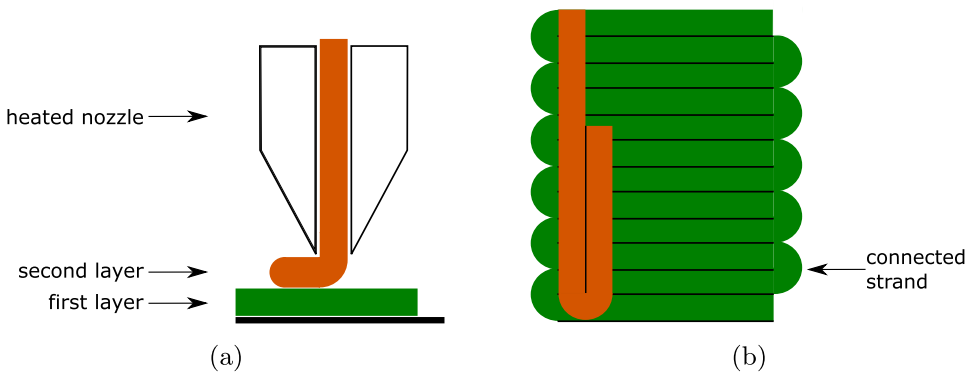

Fig. 1 FFF printing process **a** from the side view and **b** from the top view (without the nozzle)

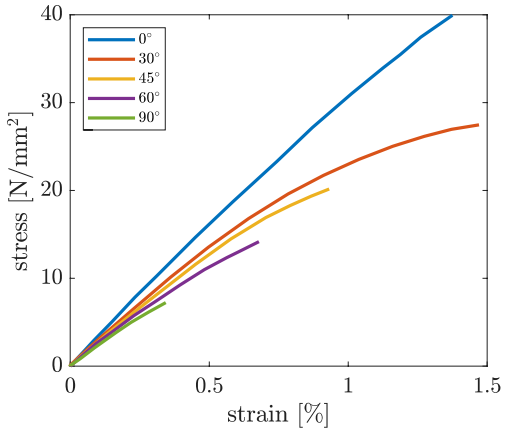

Fig. 3 Experimental results of unidirectional layup [8]

means different mechanical properties for the printed object at the end. In this work, the focus is on PLA.

2.2 Numerical model

In this section, the modelling assumptions and numerical setup for the simulations are explained. Ansys© Mechanical Enterprise, Release 22.2 [20] is the commercial FE software that was used for the simulations. All simulations were performed on a Linux HPC cluster using parallel computing with up to 192 processors. All challenges are briefly explained and a possible approach to the problem is outlined.

To resolve the mesostructure of the tensile specimen, each strand is modelled individually and an octagon cross-section is used to approximate the oval shape of the printed strand as shown in Fig. 4.

To determine the factors c_v and c_h, that are multiplied with the width a respectively height b, a microscope image of a cross-section of a specimen after failure is used and the factors are measured and averaged over several strands. Details will be explained in the Sect. 2.2.1.

Experimental tests with unidirectional PLA specimens have shown a rather brittle material behaviour, as can be seen in the stress–strain diagram in Fig. 3 and in the fracture surface shown in Fig. 5. Accordingly, linear isotropic

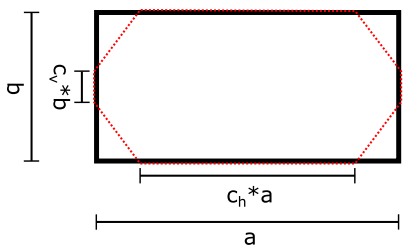

Fig. 4 Approximation of strand's geometry

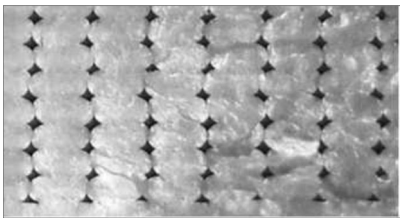

Fig. 5 Fracture image of a 0° tensile specimen

elastic material behaviour with a brittle failure is assumed. To describe this material behaviour, only the three material parameters Young's modulus E, Poisson's ratio ν and the strength σ_f are required. These are determined using reference tests in Sect. 2.2.2.

Since a large number of elements are required for a detailed resolving of the mesostructure, only one layer and only a part of the specimen are simulated. This is described in more detail in Sect. 2.2.4. For the fracture, the techniques of Element Erosion and Element Deletion are presented in Sect. 2.2.3 and discussed in Sect. 3.1. These are simulation techniques in which the stiffness of an element is greatly reduced in the case of Element Erosion or the entire element is deleted in the case of Element Deletion once a user-defined criterion has been reached. Different equivalent stresses (von Mises equivalent stress and maximum-normal stress), which calculate the criterion for the failure, are presented in Sect. 2.2.2 and discussed in Sect. 3.2. In addition, case studies on the different designs and their influences of the specimen's edges are performed. It is possible to model the connected strands true to detail, to model the strands slightly offset to each other or the influence of the edge is negligible and no additional edge is modelled. The comparison is made in Sect. 3.3.

2.2.1 Geometry

The strands in [8] were printed with a width $a = 0.4$ mm and a height of $b = 0.2$ mm.

If we look at the contact lengths of all the strands shown in Fig. 5 and average them, we get on average a value of $c_h = 0.72$ and $c_v = 0.36$. While the scatter of the horizontal contact length is very small with a standard deviation of $\sigma = 0.032$, the value for the vertical contact length scatters much more with a standard deviation of $\sigma = 0.066$. Zones in which the strands from two different layers touch are called interlayer zones, whereas zones in which two strands from one layer touch are called intralayer zones. It has been shown experimentally e.g. in [8, 9, 12] that unidirectional specimen typically fail due to intralayer debonding, unless loading is parallel to the strand orientation.

Figure 4 shows the approximated shape of the strand. Every strand is resolved uniformly and small differences

of different strands resulting from the printing process are neglected. The contact length c_v has an high influence on the failure and on the material response on a macroscopic level e.g. the strength σ_f, as explained later in Sect. 3.4. The most simplified form to capture these effects is the octagon to approximate the strand. a and b correspond to the width and height of the printed specimen, that are set in the slicer for 3D printing. It is known that the material strength in the intralayer zones is generally lower than in the bulk of the strands due to limited molecular diffusion between strands during printing [21–23]. For taking into account, the strength is reduced in the intralayer zones, the vertical contact length c_v, which was determined optically in Sect. 2.2.1 is reduced, as shown in detail in Sect. 3.4.

2.2.2 Material model

For a linear elastic material model with brittle failure, three material parameters are required. While the Poisson's ratio ν is taken from the literature as $\nu = 0.3$ like in [24], the Young's modulus E and the strength σ_f are taken from the experiments from [8] shown in Fig. 3, more precisely, from the 0° case. It has to be noted that in [8], stresses were calculated from the measured force assuming a solid rectangular cross-section of the specimen (ignoring the voids). Therefore, stiffness and strength for our model with the octagon cross-section of the strands (see Fig. 4) are obtained by scaling the values extracted from Fig. 3 by the ratio

$$\frac{A_{\text{rec}}}{A_{\text{oct}}}, \tag{1}$$

where $A_{\text{rec}} = a \cdot b$ is the cross-sectional area of a simplified, rectangular shape of a strand, and A_{oct} is the cross-sectional area of the octagon shape in Fig. 4. With $c_h = 0.7$ and $c_v = 0.2$, that are initially chosen under the assumptions (reduced strength in the intralayer zones) from Sect. 2.2.1, we obtain

$$\frac{A_{\text{rec}}}{A_{\text{oct}}} = 1.136. \tag{2}$$

Accordingly, the Young's modulus and strength for the simulation models are obtained as

$$E_{\text{sim}} = 1.136 \cdot E_{\text{exp}} \tag{3}$$

$$\sigma_{f,\text{sim}} = 1.136 \cdot \sigma_{f,\text{exp}}, \tag{4}$$

where E_{exp} and $\sigma_{f,\text{exp}}$ are the values obtained from the 0° specimen experimental curve in Fig. 3.

All material parameters for all upcoming simulations are summarized in Table 1.

Table 1 Material parameters

E_{sim}	ν_{sim}	$\sigma_{f,\text{sim}}$
3901 MPa	0.3	45.38 MPa

Since 3D solid elements are used in the simulations, an equivalent stress measure is needed for the failure criterion. Two different equivalent stresses are used and compared for the subsequent numerical implementation. Equivalent stresses can be calculated with the help of the principal stresses σ_{I}, σ_{II} and σ_{III}. Besides the von Mises equivalent stress

$$\sigma_{\text{eqv,vM}} = \sqrt{\frac{(\sigma_{\text{I}} - \sigma_{\text{II}})^2 + (\sigma_{\text{II}} - \sigma_{\text{III}})^2 + (\sigma_{\text{III}} - \sigma_{\text{I}})^2}{2}}, \tag{5}$$

which is particularly suitable for ductile materials [25], the maximum-normal stress hypothesis is used for brittle materials and/or rapid loading [26–28]. The maximum-normal stress hypothesis also known as Rankine's theory [29] calculates the equivalent stress for tension-dominated stress states ($\sigma_{\text{I}} \geq 0$ and $\sigma_{\text{I}} \geq |\sigma_{\text{III}}|$) as

$$\sigma_{\text{eqv,R}} = \sigma_{\text{I}} \tag{6}$$

as a criterion for failure.

2.2.3 Simulation of the fracture

To simulate failure Ansys© offers the Element Birth and Death technology, also known as Element Erosion (EE) [30]. Since this technique can lead to convergence problems (see Sect. 3.1), we developed an alternative approach in which failure is represented with deleted elements instead of eroded elements. For this purpose, data like element numbers, material parameters, previous computed results etc. must be temporarily stored after each load step/iteration (if failure happens) and transferred to a new mesh. The next load step/iteration is then computed with a new mesh. We call this technique Element Deletion (ED). The principle of these two methods are explained in the following for pointing out the differences.

After an initial simulation, each element is checked in post-processing for exceeding a freely selectable criterion. This criterion can be e.g. equivalent stresses, strains or any other user-defined criterion. If the element exceeds this limit, the element will be "killed" or deleted. It is important to know that "killing" the element does not mean that the element is completely deleted, but the element stiffness is multiplied with the factor 10^{-6}. Thus the element still exists in contrast to ED, where the whole element is completely deleted.

The advantages of EE are:

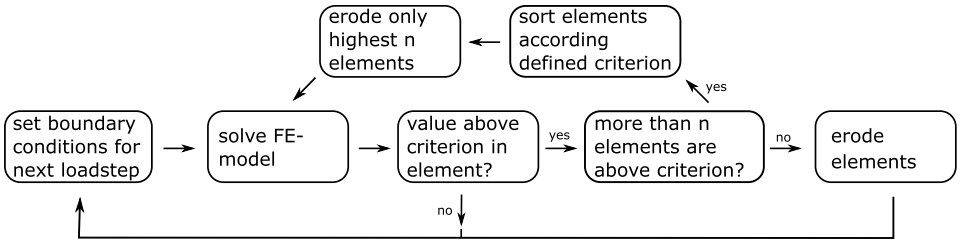

Fig. 6 Extended scheme for an EE simulation with localization

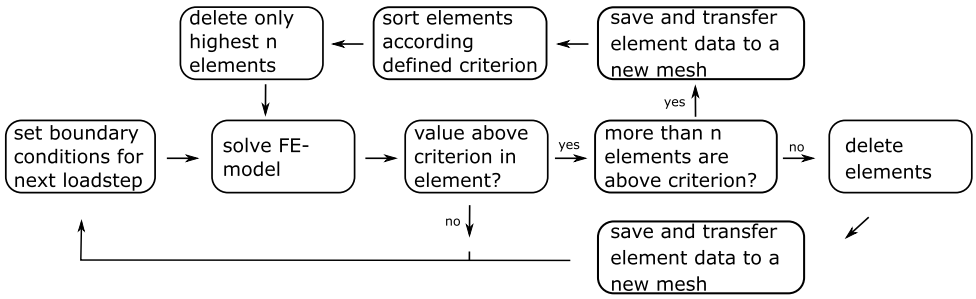

Fig. 7 Extended scheme for an ED simulation with localization

- continuous connectivity of the FE mesh
- visualization of the failed elements.

Whereas the disadvantages for EE are:

- excessive element distortion of eroded elements, although physically irrelevant, can lead to abortion of the simulation.

The advantages and disadvantages for ED are vice versa. It is noted, that both techniques were used for the simulations and both lead almost to the same results and are shown in Sect. 3.1.

Due to the uniform stress state in these simulations, many elements exceed the failure criterion at the same time. This occurs mainly at the intralayer zones. To prevent all intralayer zones from failing at the same time the failure must be localized. To implement this localization, the software's workflow is extended and shown in Fig. 6 for EE and in Fig. 7 for ED.

If the element solution of at least one element exceeds the user-defined criterion, all elements that exceed this criterion are sorted in descending order. In order to achieve localization, not all elements may be "killed" or deleted, but only the n elements, that exceed the criterion value the highest. The amount n must be chosen sensibly so that neither too few elements are "killed" or deleted and the simulation becomes too expensive, nor too many elements are "killed" or deleted and no localization takes place. In the simulations in Sect. 3, a value of 0.01% of the total number of elements was selected for n.

2.2.4 Mesh

The mesh for the FE simulations was created directly in the simulation software Ansys©. A 3-D 8-node solid element using the $\overline{B}$-method with full integration was used. The converge criteria are 0.5% for displacements and forces to ensure a realistic and valid outcome. Every node has three degrees of freedom, that are the translations in x, y and z direction. Our models do not simulate the whole dogbone from [8], but only one layer and a smaller part shown in Fig. 8 to reduce the amount of elements. At the upper and lower ends, the displacement in the x-direction is fixed in the centre and the displacement in the y-direction is fixed at the respective corners. In addition, the entire upper edge is fixed in the z-direction and the displacement is applied in every loadstep to the lower edge until the specimen fails. The left and right edge are traction free. The boundary conditions are shown in Fig. 8.

Requirements for the mesh for the simulations of the mesostructure are, on the one hand, to limit the number of

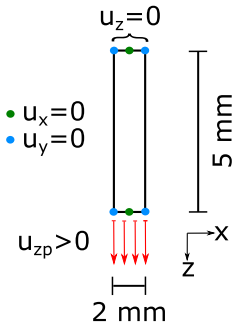

Fig. 8 Simulated part of the specimen including boundary conditions

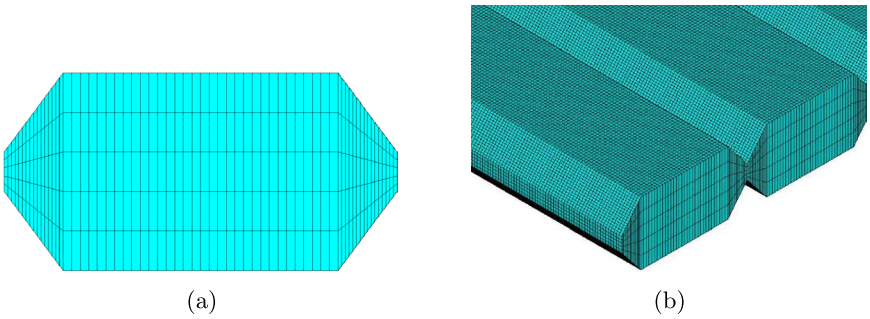

Fig. 9 **a** Mesh of a strand cross-section with 320 8-node hexaeder and **b** section of the entire mesh

elements upwards so that the simulation does not become too expensive, but on the other hand, to have the mesh fine enough for representing failure by narrow zones of eroded/deleted elements, avoiding too much "loss" of material. The mesh of a cross-section and a section of the entire mesh are shown in Fig. 9. The simulation models have an average total number of 500,000 elements. The exact number of elements depends on the angle of the strands to the loading direction. The average calculation time of a model on 96 processors on the cluster is approximately 24 h. The central area of the dogbone in [8] has a dimension of 10 mm · 50 mm. To simulate the entire dogbone for our studies, the number of elements would be in the tens of millions, which would not be practical.

3 Results and discussion

This section presents the results of the simulations and parameter studies. Firstly, the techniques EE and ED, the different stress hypotheses plus the influence of the specimen's edge are discussed in order to qualitatively build the model. Secondly, the model is then finally calibrated using the contact lengths c_v and c_h. All experiments that are simulated are from [8], that are shown in Fig. 3.

3.1 Element erosion vs. element deletion

Simulations were carried out using both the EE technique and the ED technique, and the results are discussed in the following. The failure patterns and the corresponding stress–strain-diagram obtained with EE simulations are shown in Figs. 10 and 11, those obtained with ED in Figs. 12 and 13.

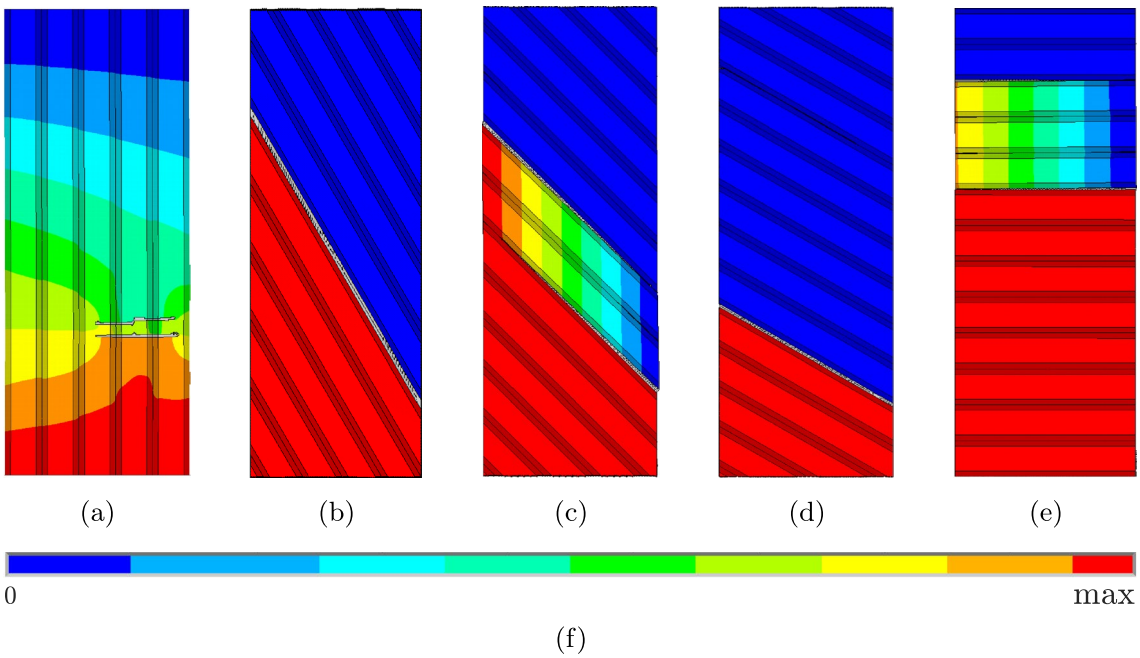

Fig. 10 Failure patterns for the simulations for **a** 0°, **b** 30°, **c** 45°, **d** 60°, and **e** 90° for the EE-technique. The colorbar **f** shows the displacement in loading direction

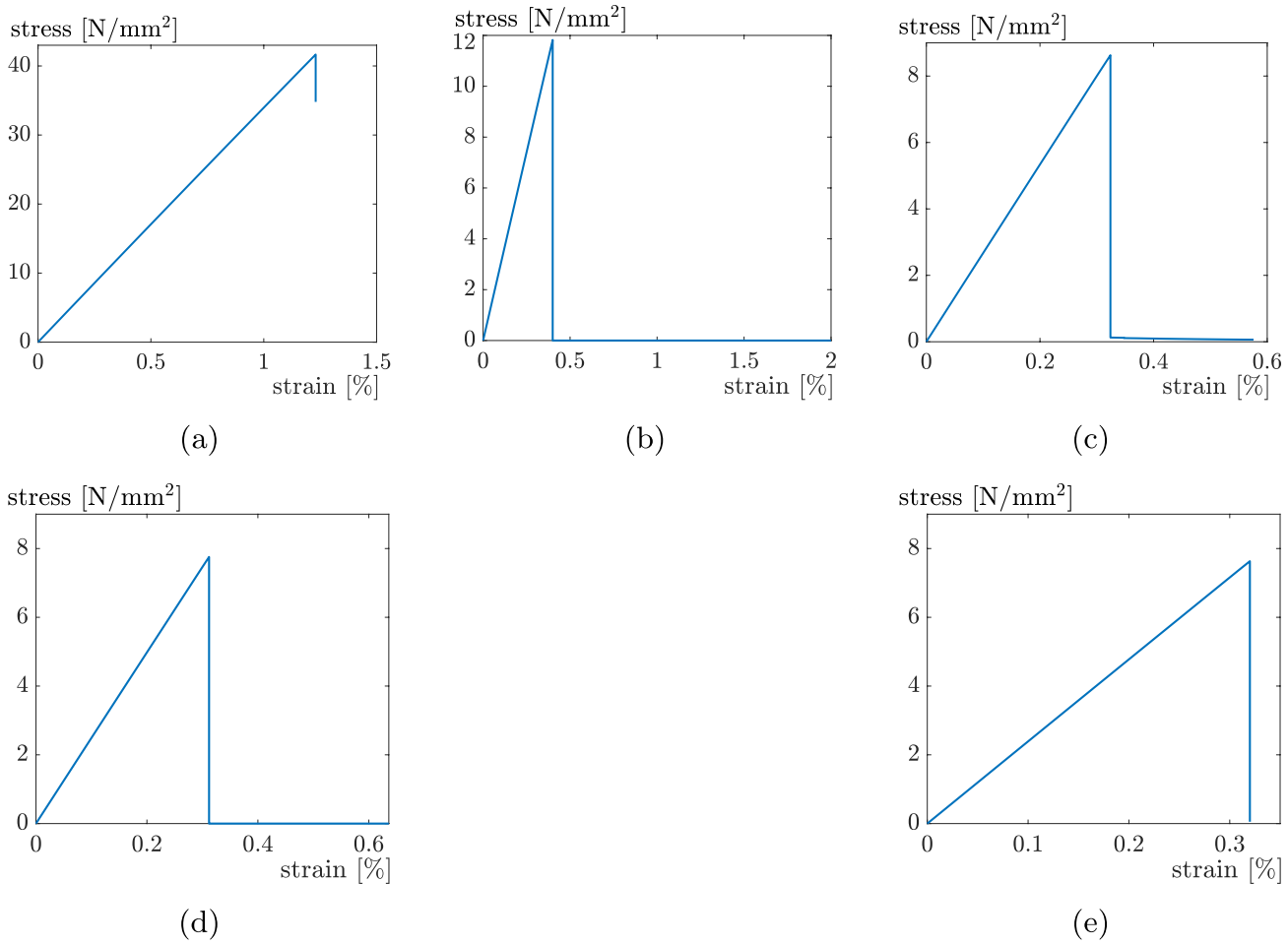

Fig. 11 Stress–strain diagrams for the simulations for **a** 0°, **b** 30°, **c** 45°, **d** 60°, and **e** 90° using the EE-technique

In general, both methods lead to very similar results, which are also consistent with the experimental findings from [8], in the sense that fracture always occurs in the intralayer zones except for the 0° case. The only difference is that the failure "jumps" from one intralayer zone to a neighbouring intralayer zone in the experiments. This could be related to the turnarounds or pre-damage from the printing process. For global failure to occur for the specimen, it seems that the "jump" from two neighbouring intralayer zones needs less energy then failure through the turnaround at the specimen's edge. Additionally [8] shows that the maximum stress decreases with increasing angle between strand orientation and loading direction, which can be simulated qualitatively as well with the presented approach. However, only with ED, it is possible to simulate all experiments until complete failure, while with EE, the simulations are often terminated before final failure of the specimens. This can be seen most clearly for the 0° case. Figure 10a shows the crack pattern from the last successful simulation step. It can be seen, that the specimen is still far away from being completely broken, there are two cracks covering only approximately half of the specimen's width. It can also be seen in Fig. 11a, where the stress–strain curve stops shortly after reaching the maximum stress, still representing a stress value of approx. 35 MPa. The same problem can be seen in Fig. 10c and e. In these cases, two cracks have developed, but none of them is going completely through the specimen, and the upper and lower parts of the specimen are still connected. This is confirmed by the stress–strain curves in Fig. 11c and e, where the curves stop shortly before reaching $\sigma = 0$. Only for the 30° and 60° cases, the simulations can run until complete failure, which can be seen in Fig. 10b and d, where the specimen is clearly broken in two parts, and in the curves in Fig. 11b and d, dropping down to $\sigma = 0$.[1] In all the cases, which do not reach the final failure, the simulations are terminated by the FE software due to excessively distorted elements within the fractured zone. Unfortunately, there is no option

[1] It's not completely zero due the very low stiffness in the eroded elements.

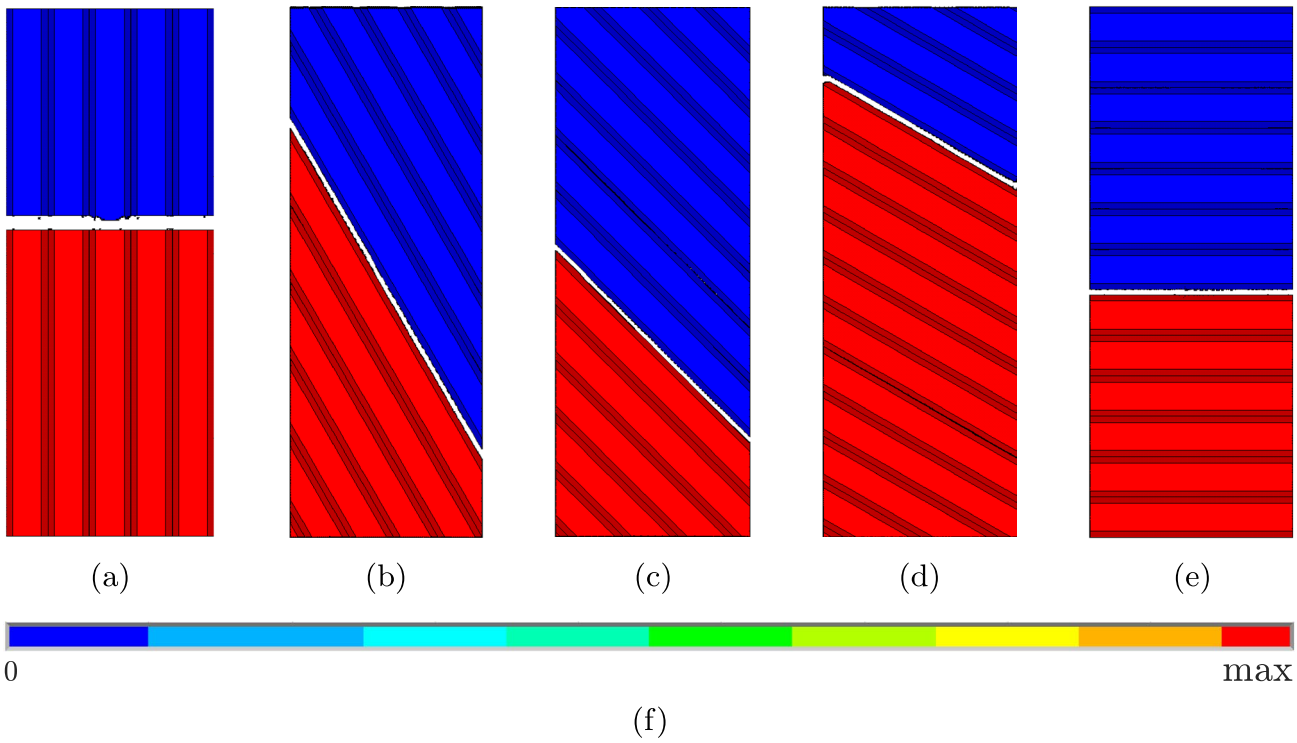

Fig. 12 Failure patterns for the simulations for **a** 0°, **b** 30°, **c** 45°, **d** 60°, and **e** 90° for the ED-technique. The colorbar **f** shows the displacement in loading direction

to ignore these elements in the distortion check. With ED instead the elements in the fractured zone are removed from the mesh and have no effect on the further simulation. As a consequence the simulations can run until complete failure of the specimens for all cases, as can be seen in Figs. 12 and 13. The global failure only appears between one intralayer zone, but there are many different areas of different intralayer zones where local failure occurs. This can be seen, for example, in the failure patterns using the EE technique in Fig. 10, as well as in Digital Image Correlation images as showed in [31]. After failure occurs these areas are difficult to recognize visually without any further post-processing using the ED technique due to a very small element size. From this study we can conclude, that the ED technique is more robust and better suited for these kind of simulations than EE, if the goal is to simulate the specimen's behaviour until complete failure.

3.2 von Mises equivalent stress vs. Rankine equivalent stress

In this section, a numerical study comparing two different equivalent stress measures as failure criteria, namely the von Mises (Eq. 5) and Rankine (Eq. 6) equivalent stresses, is performed in order to find out which one is best suited to replicate the failure behaviour of FFF specimens observed in [8]. Figure 14 shows the stress–strain curves for all specimens $(0°, 30°, 45°, 60°, 90°)$ obtained with (a) Rankine equivalent stress and (b) von Mises equivalent stress. It is noted, that in both cases the curves do not perfectly match with the experimental curves in [8]. In general, it can be seen that the experiment from Fig. 3 does not have a linear curve, but a slightly curved curve in the stress–strain diagram. However, with the Rankine equivalent stress as failure criterion, the results (Table 2) correctly represent the general trend that the maximum stress decreases with increasing angle between loading direction and strand orientation. Instead with the von Mises failure criterion the 90° specimen exhibits a higher strength than the 60° and 45° cases, which is in contrast to the experiment in [8].

The brittle behaviour at failure of the experiments [8] and the decreasing of the material parameters E and $\sigma_{f,\mathrm{sim}}$ are better simulated by the Rankine hypothesis.

3.3 Modelling of the specimen's edge

Since the FE-models represent the mesostructure, the question arises as to whether the edges have an influence on the simulations, as edges in the printed specimen are usually the initiation for a crack. Typically, the printing in the FFF results in connecting printed material between two strands,

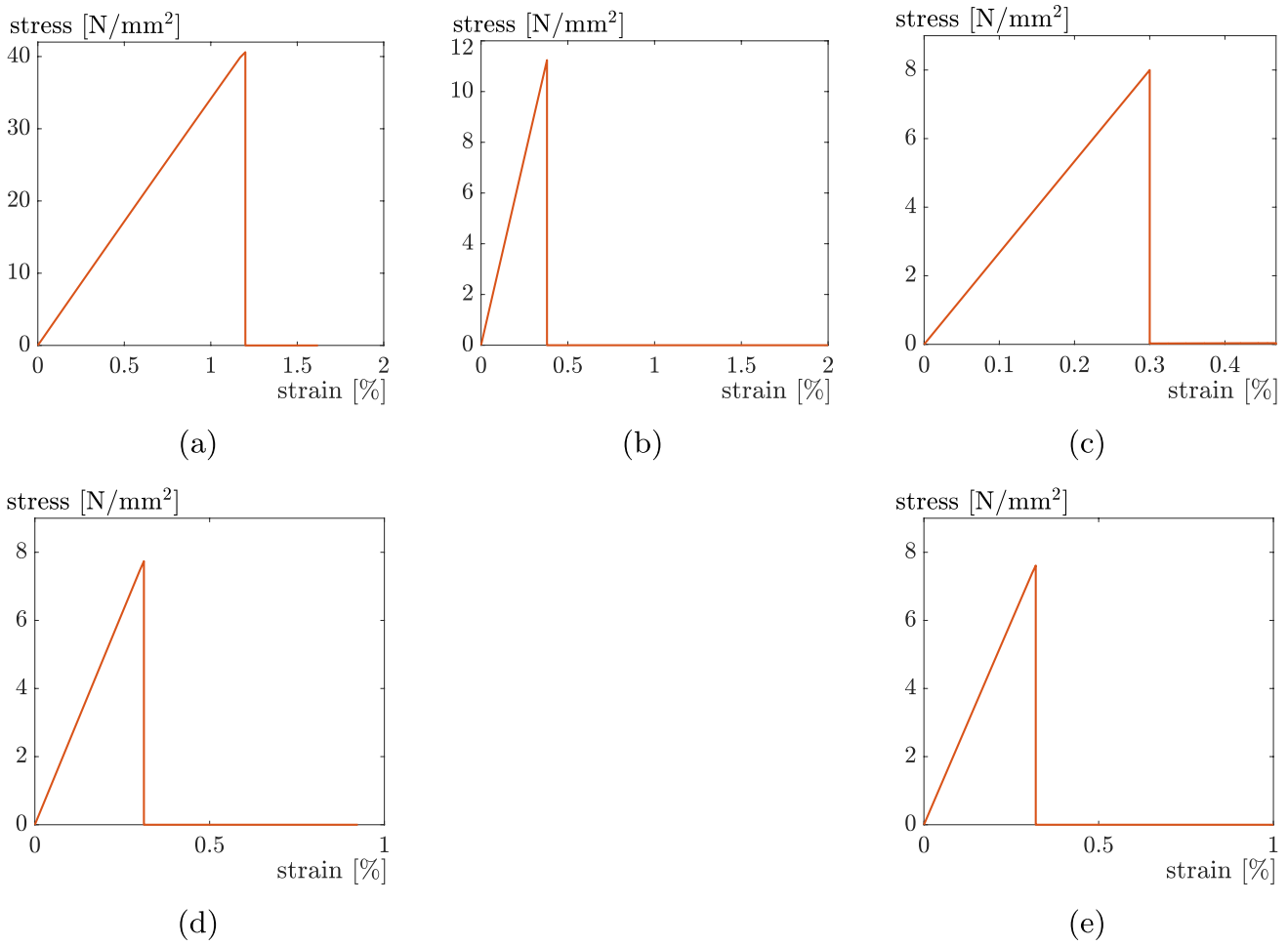

Fig. 13 Stress–strain diagrams for the simulations for **a** 0°, **b** 30°, **c** 45°, **d** 60°, and **e** 90° using the ED-technique

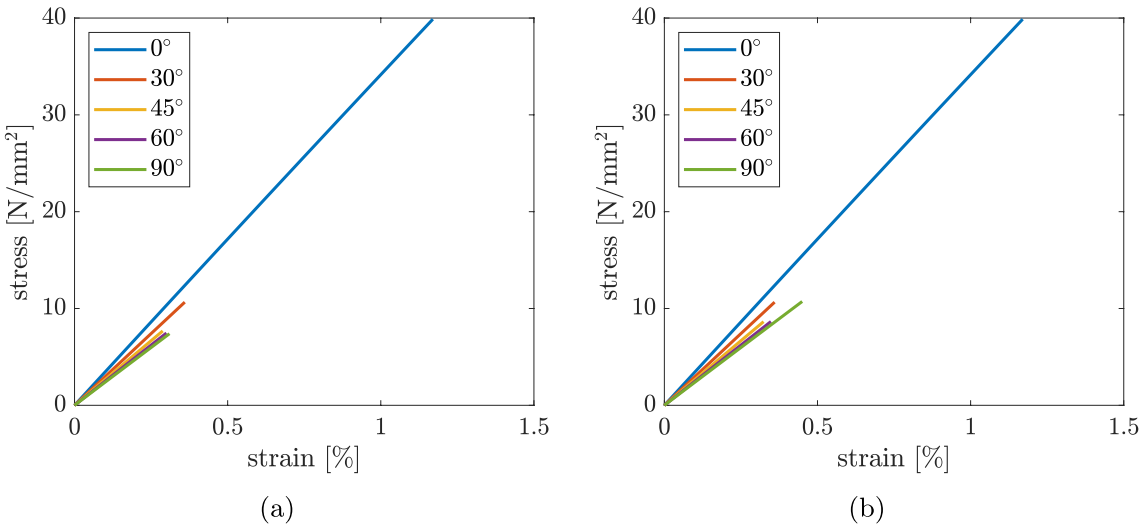

Fig. 14 Stress–strain diagrams using **a** Rankine equivalent stress, **b** von Mises equivalent stress

Table 2 Material parameter E [MPa] and σ_f [MPa] of the experiments and simulations

	0°	30°	45°	60°	90°
E_{exp}	3434	2762	2627	2334	2337
E_{sim} (von Mises)	3439	2962	2667	2488	2385
E_{sim} (Rankine)	3439	2962	2667	2488	2385
$\sigma_{f,\text{exp}}$	39.95	27.47	20.16	14.17	7.24
$\sigma_{f,\text{sim}}$ (von Mises)	39.88	10.65	8.63	8.65	10.72
$\sigma_{f,\text{sim}}$ (Rankine)	39.88	10.65	7.68	7.46	7.39

even if retraction is set in the slicer. These connections between the two strands cannot be avoided and could therefore potentially have an influence on the failure. A microscope image of the edges of a 90° specimen is depicted in Fig. 15a, showing the typical "turnarounds" which are the result of the continuous print path. Since the geometry creation and meshing of these turnarounds is not trivial, especially for the non-90° cases, different ways of modelling with different level of simplification as shown in Fig. 15b–d are tested in the following. Figure 15b represents the reference model, where the turnarounds are modelled in detail. Figure 15c is a simplified model without turnarounds, but at the edge is always a slight offset between two neighbouring strands. The idea of this offset is to have reentrant corners, which create stress concentrations, that might have a similar effect as the reentrant corner between two turnarounds. Lastly, Fig. 15d shows the most simplified model without turnarounds and a smooth edge.

Figure 16 shows the maximum stress obtained with the different types of modelling the edges. Noteworthy, the additional material at the edge (connecting strands/turnrounds) has only a minor influence of 5% on $\sigma_{f,\text{sim}}$ compared to the specimen without connecting strands. The staggered strands have a 25% lower $\sigma_{f,\text{sim}}$ and therefore a too big influence compared to the connecting strands. Therefore, due to the simpler modelling, it is recommended to carry out the simulations with an edge without turnarounds.

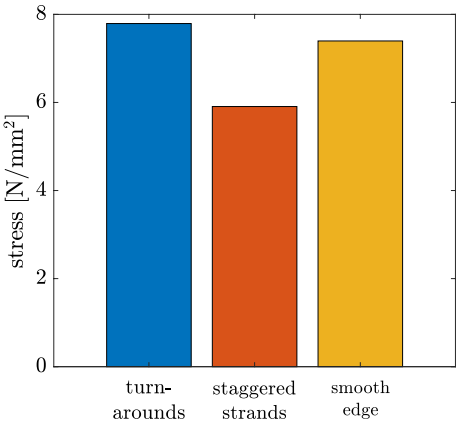

Fig. 16 Maximum stress for the different types of modelling the edges of the 90° specimen

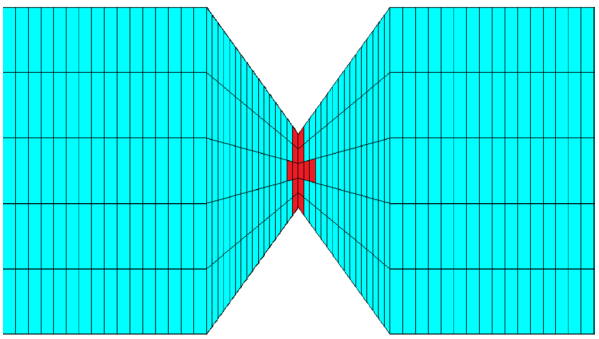

Fig. 17 Side view of the intralayer zone of a 90° specimen. Deleted elements after failure are colored in red

3.4 Intralayer zone

In Sect. 2.2.4, the importance of the fineness of the mesh, especially in the intralayer zone, is described. Since the intralayer zone is responsible for the failure in all cases except for the 0° specimen, it is important that only very few elements are deleted upon failure due to fine meshing. As shown in Fig. 17 only one and a maximum of up to

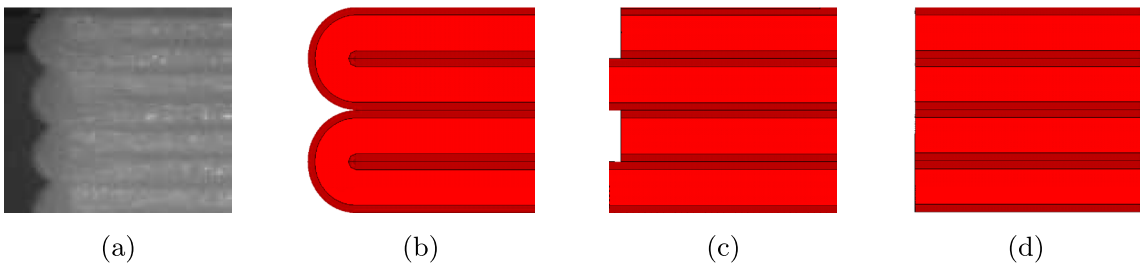

Fig. 15 Edge of the 90° specimen for **a** the experiment, **b** the simulation with turnarounds, **c** the simulation with staggered strands by two elements, and **d** the simulation with non-staggered strands without turnarounds

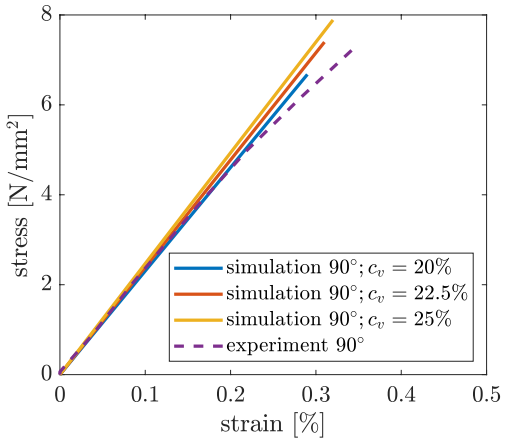

Fig. 18 Stress–strain diagrams for a 90° specimen with various c_v

three elements are deleted per cross-section of one strand, which corresponds to only 1.7% and 5% respectively of the strand's width a.

As described in Sect. 2.2.1, the vertical contact length of the individual strands in the intralayer zone has to be verified. The 90° specimen is used for this, as no overlapping failure mechanisms other than the failure of the intralayer zone orthogonal to the strand are to be expected here. To ensure that the area of the strand remains constant, the horizontal contact length c_h must also be changed when the vertical contact length c_v is changed. The constant area is necessary so that the strength σ_f and Young's modulus E from Table 1 do not change for the 0° specimen. For a 90° specimen Fig. 18 shows that E and σ_f also increase with increasing c_v. The best agreement between experiment and simulation is achieved with a $c_v = 0.225$.

4 Conclusion

We have presented a finite element modelling approach for simulating the mechanical behaviour of unidirectional FFF-printed PLA specimens under tensile loading with different strand orientations. The goal was to represent the main features, which were observed experimentally in [8]. In contrast to other existing works, the focus in this paper is on the fracture behaviour, and the goal was to simulate the experiments until final failure of the specimens. In our approach, the mesostructure is resolved by using octagon cross-sections for each strand. We have shown that with such models, we can replicate the typical behaviour of FFF specimens in which failure typically happens between strands unless the strands are almost parallel to the loading direction and the specimens' strength decrease with increasing angle between loading direction and strand orientation. We have investigated several detail questions for the modelling, for example, we compared the suitability of Element Erosion and Element Deletion techniques for this kind of simulations, finding that only with Element Deletion, it was possible to simulate the loading until final failure for all cases. Furthermore, we compared different failure criteria, namely the von Mises and Rankine equivalent stresses, finding that only with Rankine equivalent stress, the simulation results show a typical behaviour, which is in accordance to experiments like those in [8, 12] or [9], of monotonic decrease in strength with increasing strand orientation angle. We have also shown that the turnarounds at the edges of FFF-printed parts can be neglected in the simulation models, which highly simplifies the model creation and meshing. These simulations form the basis for improvements such as a more complex material model for further research. Our approach can also be used to investigate the failure behaviour of more complex structures. A further step of the numerical model is the extension to cross layups and the verification of the increase in toughness as shown experimentally in [8]. Extending this approach to other filament materials, which require more complex material models like plasticity, hyperelasticity and viscoelasticity, is planned as future research. Additionally, real world problems such as load capacity, failure behaviour and location for complex FFF printed parts due to non-uniform layer orientations can be investigated with the presented approach as well.

Acknowledgements This work has received funding from the European Research Council (ERC) under the European Union's Horizon 2020 research and innovation programme (Grant agreement no. 864482) and dtec.bw—Digitalization and Technology Research Center of the Bundeswehr. dtec.bw is funded by the European Union NextGenerationEU fund. The financial support by Universität der Bundeswehr München enabled open access publishing. Images used courtesy of ANSYS, Inc. All the support is gratefully acknowledged.

Funding Open Access funding enabled and organized by Projekt DEAL.

Data availability The data that support the findings of this study are available from the corresponding author upon reasonable request.

Declarations

Conflict of interest On behalf of all authors, the corresponding author states that there is no Conflict of interest.

References

1. Khosravani MR, Soltani P, Rolfe B, Reinicke T, Zolfagharian A (2024) Static and dynamic characterization of 3D-printed polymer structural elements. Polym Test. https://doi.org/10.1016/j.polymertesting.2024.108533
2. Djokikj J, Tuteski O, Doncheva E, Hadjieva B (2022) Experimental investigation on mechanical properties of FFF parts using different materials. Elsevier B.V., Amsterdam. https://doi.org/10.1016/j.prostr.2022.05.076
3. Butt J, Bhaskar R, Mohaghegh V (2022) Analysing the effects of layer heights and line widths on FFF-printed thermoplastics. Int J Adv Manuf Technol 121:7383–7411. https://doi.org/10.1007/s00170-022-09810-z
4. Popescu D, Zapciu A, Amza C, Baciu F, Marinescu R (2018) FDM process parameters influence over the mechanical properties of polymer specimens: a review. Polym Test 69:157–166. https://doi.org/10.1016/j.polymertesting.2018.05.020
5. Yan J, Demirci E, Ganesan A, Gleadall A (2022) Extrusion width critically affects fibre orientation in short fibre reinforced material extrusion additive manufacturing. Addit Manuf. https://doi.org/10.1016/j.addma.2021.102496
6. Petousis M, Vidakis N, Mountakis N, Karapidakis E, Moutsopoulou A (2023) Compressive response versus power consumption of acrylonitrile butadiene styrene in material extrusion additive manufacturing: the impact of seven critical control parameters. Int J Adv Manuf Technol 126:1233–1245. https://doi.org/10.1007/s00170-023-11202-w
7. Khosravani MR, Zolfagharian A, Jennings M, Reinicke T (2020) Structural performance of 3D-printed composites under various loads and environmental conditions. Polym Test. https://doi.org/10.1016/j.polymertesting.2020.106770
8. Kiendl J, Gao C (2020) Controlling toughness and strength of FDM 3D-printed PLA components through the raster layup. Compos Part B: Eng. https://doi.org/10.1016/j.compositesb.2019.107562
9. Khosravani MR, Berto F, Ayatollahi MR, Reinicke T (2022) Characterization of 3D-printed PLA parts with different raster orientations and printing speeds. Sci Rep. https://doi.org/10.1038/s41598-022-05005-4
10. Zhang G, Wang Q, Ni Y, Liu P, Liu F, Leguillon D, Xu LR (2023) A systematic investigation on the minimum tensile strengths and size effects of 3D printing polymers. Polym Test. https://doi.org/10.1016/j.polymertesting.2022.107845
11. Song Y, Li Y, Song W, Yee K, Lee KY, Tagarielli VL (2017) Measurements of the mechanical response of unidirectional 3D-printed PLA. Mater Des 123:154–164. https://doi.org/10.1016/j.matdes.2017.03.051
12. Yao T, Ye J, Deng Z, Zhang K, Ma Y, Ouyang H (2020) Tensile failure strength and separation angle of FDM 3D printing PLA material: experimental and theoretical analyses. Compos Part B: Eng. https://doi.org/10.1016/j.compositesb.2020.107894
13. Alaimo G, Marconi S, Costato L, Auricchio F (2017) Influence of meso-structure and chemical composition on FDM 3D-printed parts. Compos Part B: Eng 113:371–380. https://doi.org/10.1016/j.compositesb.2017.01.019
14. Li L, Sun Q, Bellehumeur C, Gu P (2002) Composite modeling and analysis for fabrication of FDM prototypes with locally controlled properties. J Manuf Process 4:129–141. https://doi.org/10.1016/S1526-6125(02)70139-4
15. Gonabadi H, Chen Y, Yadav A, Bull S (2022) Investigation of the effect of raster angle, build orientation, and infill density on the elastic response of 3D printed parts using finite element microstructural modeling and homogenization techniques. Int J Adv Manuf Technol 118:1485–1510. https://doi.org/10.1007/s00170-021-07940-4
16. Somireddy M, Czekanski A, Singh CV (2018) Development of constitutive material model of 3D printed structure via FDM. Mater Today Commun 15:143–152. https://doi.org/10.1016/j.mtcomm.2018.03.004
17. Völkl H, Mayer J, Wartzack S (2020) Strukturmechanische Simulation additiv im FFF-Verfahren gefertigter Bauteile. Springer, Berlin. https://doi.org/10.1007/978-3-662-61149-4_10
18. Wendt C, Valerga AP, Droste O, Batista M, Marcos M (2017) Fem based evaluation of fused layer modelling monolayers in tensile testing. Procedia Manuf 13:916–923. https://doi.org/10.1016/j.promfg.2017.09.160
19. Garg A, Bhattacharya A (2017) An insight to the failure of FDM parts under tensile loading: finite element analysis and experimental study. Int J Mech Sci 120:225–236. https://doi.org/10.1016/j.ijmecsci.2016.11.032
20. ANSYS I (2022) Ansys academic research mechanical, release 22.2. http://www.ansys.com. Accessed 23 Oct 2023
21. Li H, Wang T, Sun J, Yu Z (2018) The effect of process parameters in fused deposition modelling on bonding degree and mechanical properties. Rapid Prototyp J 24:80–92. https://doi.org/10.1108/RPJ-06-2016-0090
22. Balani SB, Mokhtarian H, Coatanéa E, Chabert F, Nassiet V, Cantarel A (2023) Integrated modeling of heat transfer, shear rate, and viscosity for simulation-based characterization of polymer coalescence during material extrusion. J Manuf Process 90:443–459. https://doi.org/10.1016/j.jmapro.2023.02.021
23. Coogan TJ, Kazmer DO (2020) Prediction of interlayer strength in material extrusion additive manufacturing. Addit Manuf. https://doi.org/10.1016/j.addma.2020.101368
24. Mirkhalaf SM, Fagerström M (2021) The mechanical behavior of polylactic acid (PLA) films: fabrication, experiments and modelling. Mech Time Depend Mater 25:119–131. https://doi.org/10.1007/s11043-019-09429-w
25. Mises R (1913) Mechanik der festen körper im plastisch- deformablen zustand. In: Nachrichten von der Gesellschaft der Wissenschaften zu Göttingen, Mathematisch-Physikalische Klasse. PPN252457811_1913. http://resolver.sub.uni-goettingen.de/purl?PPN252457811_1913
26. Hearn EJ (1997) Chapter 15—Theories of elastic failure. Butterworth-Heinemann, Oxford. https://doi.org/10.1016/B978-0750632652-50016-5
27. Sackey SM, Ngewana TZ (2022) Concept of equivalent stress criterion for predicting failure of brittle materials. Afr J Appl Res 8:332–343. https://doi.org/10.26437/ajar.31.10.2022.23
28. Gu J, Chen P (2018) A failure criterion for homogeneous and isotropic materials distinguishing the different effects of hydrostatic tension and compression. Eur J Mech A/Solids 70:15–22. https://doi.org/10.1016/j.euromechsol.2018.01.013
29. Rankine WJM (1857) On the stability of loose earth. Philos Trans R Soc Lond 147:9–27
30. ANSYS I (2022) Ansys academic research mechanical, release 22.2, help system, birth and death technology
31. Cunha FG, Santos TG, Xavier J (2021) In situ monitoring of additive manufacturing using digital image correlation: a review. MDPI AG. https://doi.org/10.3390/ma14061511